CM² MAGAZINE

第 4 期

南方科技大学海洋磁学中心主编

创刊词

海洋是生命的摇篮，是文明的纽带。地球上最早的生命诞生于海洋，海洋里的生命最终进化成了人类，人类的文化融合又通过海洋得以实现。人因海而兴。

人类对海洋的探索从未停止。从远古时代美丽的神话传说，到麦哲伦的全球航行，再到现代对大洋的科学钻探计划，海洋逐渐从人类敬畏崇拜幻想的精神寄托演变成可以开发利用与科学研究的客观存在。其中，上个世纪与太空探索同步发展的大洋科学钻探计划将人类对海洋的认知推向了崭新的纬度：深海（deep sea）与深时（deep time）。大洋钻探计划让人类知道，奔流不息的大海之下，埋藏的却是亿万年的地球历史。它们记录了地球板块的运动，从而使板块构造学说得到证实；它们记录了地球环境的演变，从而让古海洋学方兴未艾。

在探索海洋的悠久历史中，从大航海时代的导航，到大洋钻探计划中不可或缺的磁性地层学，磁学发挥了不可替代的作用。这不是偶然，因为从微观到宏观，磁性是最基本的物理属性之一，可以说，万物皆有磁性。基于课题组的学科背景和对海洋的理解，我们对海洋的探索以磁学为主要手段，海洋磁学中心因此而生。

海洋磁学中心，简称 CM^2，一为其全名“Centre for Marine Magnetism”的缩写，另者恰与爱因斯坦著名的质能方程 $E = MC^2$ 对称，借以表达我们对科学巨匠的敬仰和对科学的不懈追求。

然而科学从来不是单打独斗的产物。我们以磁学为研究海洋的主攻利器，但绝不仅限于磁学。凡与磁学相关的领域均是我们关注的重点。为了跟踪反映国内外地球科学特别是与磁学有关的地球科学领域的最新研究进展，海洋磁学中心特地主办 CM^2 Magazine，以期与各位地球科学工作者相互交流学习、合作共进！

“海洋孕育了生命，联通了世界，促进了发展”。 21 世纪是海洋科学的时代，由陆向海，让我们携手迈进中国海洋科学的黄金时代！

目 录

CM²快讯 1

文献导读 2

1. 侏罗纪非生物到生物的转变控制海洋生态的成功 2

2. 海相铁氧化物揭示海水氧同位素的地质历史 6

3. 定义大印度的边界 8

4. 西伯利亚 Viluy Traps 地区记录的泥盆纪地磁场的异常降低 10

5. 在冰期粉尘输送更多生物可利用的铁源到南大洋 13

6. 阿拉斯加考古炉灶的磁测：一种用来调查通往北美之路上人类存在的工具 16

7. 3200 年前地中海东岸的寒旱气候灾害的爆发 19

8. 末次盛冰期中国西北伊犁盆地大气风尘变化 21

9. 转换边缘高原 24

10. 有机碳流控制海洋沉积物中磁小体化石的形貌 26

CM^2 快讯

南科大-中大海洋磁学 2019 年学术交流会成功举行

2019 年 11 月 15 至 16 日，“南科大-中大海洋磁学 2019 年学术交流会”在南科大顺利举行。双边课题组就各自研究的领域做了深入的交流探讨。

双边课题组合影

南海是近年来地学界研究的热点。与会人员分别就南海与菲律宾海的构造演化、南海的有孔虫分布、南海记录的古地磁场强度、南海古深层流重建、南海西沙泻湖记录的热带风暴事件做了交流讨论。

石笋作为古气候的载体，近年来与磁学的结合，充分展现了其在古气候研究中的旺盛生命力。双边课题组人员就石笋磁学进行了探讨，交流了其反映的古气候信息和对华南古人类演化的研究意义。

此外，“海洋磁异常记录的白垩纪磁静期地磁场古强度的变化”、“低纬驱动 190ka 以来亚北极太平洋气候变化”、“锰结核加热形成的纳米磁性矿物的特征”、 “IRM 磁学参数分离”、“西南天山早石炭世大陆弧岩浆系统特征”、“异化铁还原菌的分离培养与矿化特征”、“基于重磁资料探讨华北克拉通的形成与破坏”的报告也在参会人员中进行了热烈探讨。

刘青松教授和杨小强教授最后对会议进行了总结。一致表示此次会议基于磁学但不限于磁学，报告主题丰富、内容详实，反映了各自课题组研究的最新进展。两大课题组应加强合作，定期互访，争取在海洋磁学研究领域合作取得优异成果。

文献导读

1. 侏罗纪非生物到生物的转变控制海洋生态的成功

翻译人：蒋晓东 jiangxd@sustech.edu.cn

Eichenseer K, Balthasar U, Smart C W, et al. ***Jurassic shift from abiotic to biotic control on marine ecological success****[J].* ***Nature Geoscience****, 2019, 12(8), 638-642.*

摘要：环境的改变和生物的相互作用均控制生物圈的演化，但这些驱动因素在地质历史时期的相对重要性仍在很大程度上是未知的。不同于环境因素，先前的研究表明生物多样性对生物圈演化的驱动效应在古生代与后古生代时期具有显著差异。海洋化学和气候对海洋钙化生态学的影响被认为在整个显生宙时期都在减弱，为验证这一假说，我们对化石记录进行系统研究。海洋钙化形成方解石或霞石的骨骼，在非生物体系中这些不同晶型碳酸钙的沉淀受控于镁钙比和温度。基于海洋化学和温度长周期的变化，我们建立环境胁迫模型，并且评估该模型在预测不同晶型碳酸钙骨骼的扩散率方面的效果。研究发现，奥陶系到中侏罗时期非生物的胁迫控制文石钙化的生态成功。这一控制机制的转变与钙化软骨在中中生代扩增完全一致。生物矿化形成的骨骼沉积到海底，缓冲 CO_2 量的漂移，使地球的生物地球化学循环趋于稳定，同时弱化了环境变化对海洋生物演化的影响。

ABSTRACT: Environmental change and biotic interactions both govern the evolution of the biosphere, but the relative importance of these drivers over geological time remains largely unknown. Previous work suggests that, unlike environmental parameters, diversity dynamics differ profoundly between the Palaeozoic and post-Palaeozoic eras. Here we use the fossil record to test the hypothesis that the influence of ocean chemistry and climate on the ecological success of marine calcifiers decreased throughout the Phanerozoic eon. Marine calcifiers build skeletons of calcite or aragonite, and the precipitation of these calcium carbonate polymorphs is governed by the magnesium-to-calcium ratio and temperature in abiotic systems. We developed an environmental forcing model based on secular changes of ocean chemistry and temperature and assessed how well the model predicts the proliferation of skeletal taxa with respect to calcium carbonate polymorphs. Abiotic forcing governs the ecological success of aragonitic calcifiers from the Ordovician to the Middle Jurassic, but not thereafter. This regime shift coincides with the proliferation of calcareous

plankton in the mid-Mesozoic. The deposition of biomineralizing plankton on the ocean floor buffers CO_2 excursions and stabilizes Earth's biochemical cycle, and thus mitigates the evolutionary impact of environmental change on the marine biota.

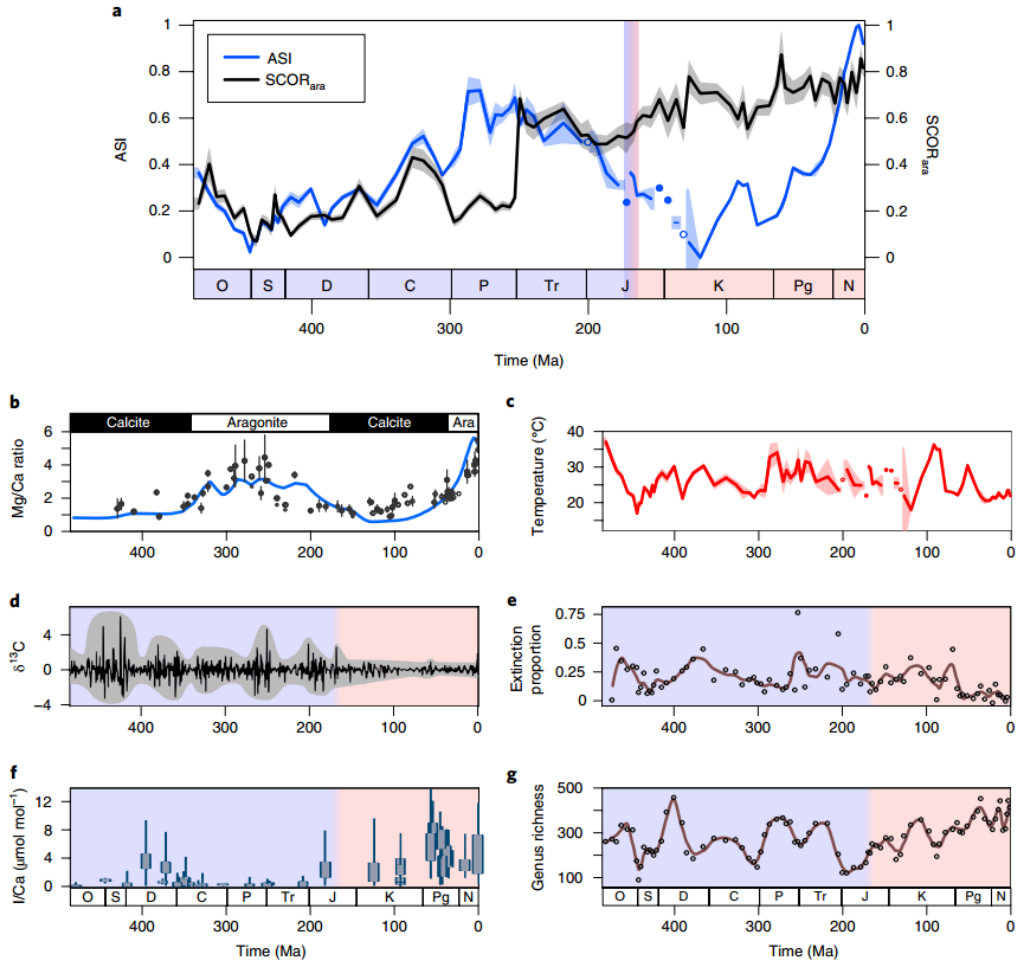

Figure 1. Environmental and biotic changes across the Ordovician-Neogene. **a**, ASI and $SCOR_{ara}$ in 85 Ordovician–Pleistocene stages. Shaded areas represent 2 s.e.m. with the ASI error envelope based on the temperature component (Methods). Solid dots show stages with only one measurement and stages without observations (circles) are averaged from the neighbouring stages. O, Ordovician; S, Silurian; D, Devonian; C, Carboniferous; P, Permian; Tr, Triassic: J, Jurassic; K, Cretaceous; Pg, Palaeogene; N, Neogene and Quaternary; Ma, million years ago. The blue-red transition and the vertical bar mark the time when the relationship between ASI and SCORara decreased most strongly (Fig. 1b, c). **b**, Modelled Mg/Ca ratio from Demicco et al. (blue line) and a compilation of Mg/Ca proxy data (black dots (Supplementary Section 1)). The bar at the top delineates calcite and aragonite sea intervals as predicted by Hardie. **c**, Mean stage-level tropical shallow water temperatures calculated from oxygen isotope measurements compiled in Veizer and Prokoph. Stages with only one measurement are drawn as solid dots, stages without observations are averaged from the neighbouring stages and are shown as circles. Shaded areas represent 2 s.e.m. **d**, Periodic changes in the envelope of third-order $\delta^{13}C$ variations, reprinted from Bachan et al. with permission of the American Journal of Science. The grey area highlights the variability. **e**, Genus-level, sampling-standardized extinction proportions (circles (Methods)) with a

long-term trend line (brown). LOESS (locally estimated scatterplot smoothing) regression with a smoothing span of 0.1. **f**, The box plots show the variability of I/Ca ratios from shallow water carbonates within sampling localities, reprinted from Lu et al. with permission from AAAS. I/Ca ratios are considered a proxy for oxygenation-higher I/Ca ratios indicate better oxygenation. **g**, Sampling-standardized marine genus-level diversity (circles (Methods)) with the long-term trend line (brown). LOESS regression with a smoothing span of 0.1.

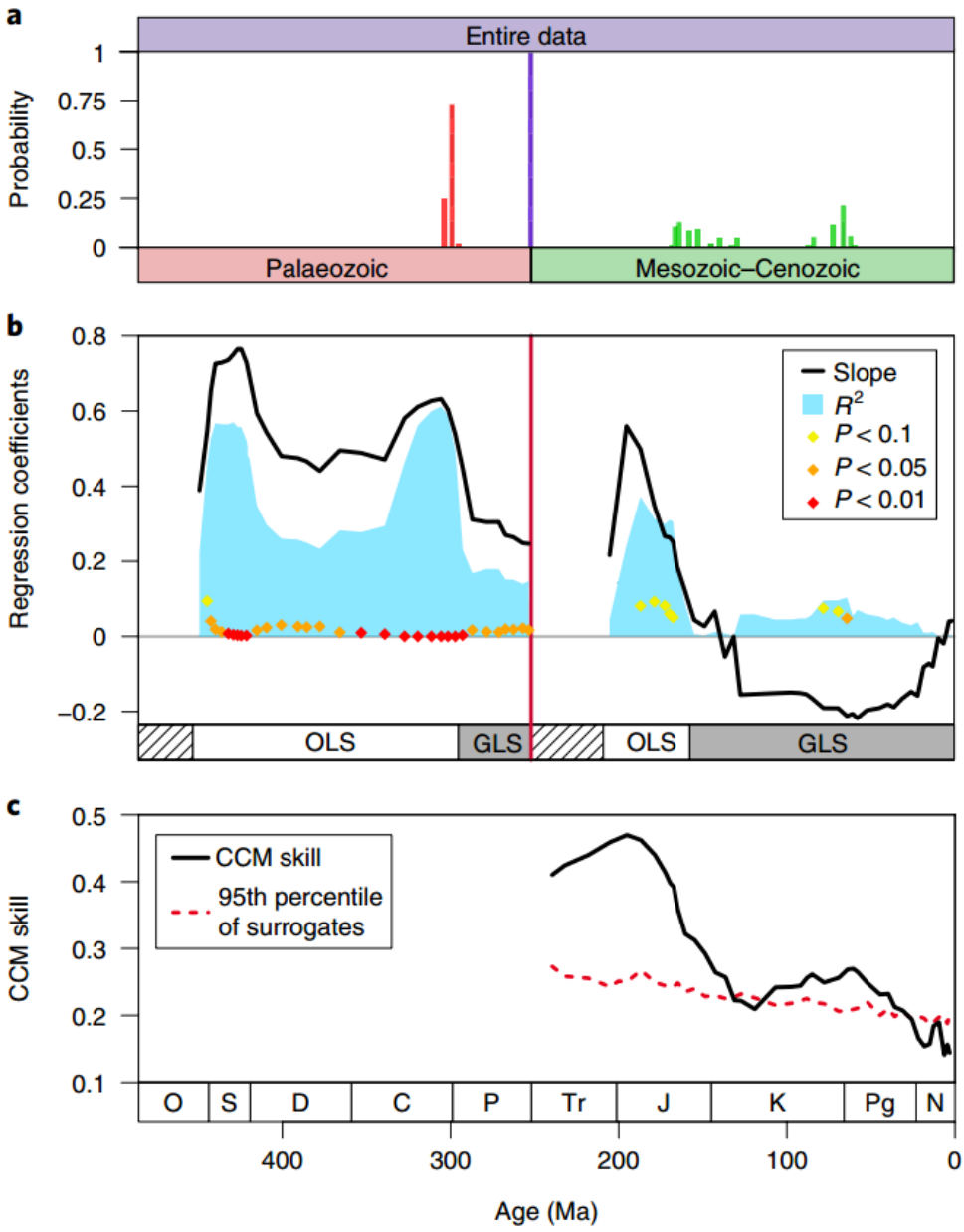

Figure 2. Changing relationship of SCorara and ASi. **a**, Bayesian posterior probabilities for changes in the linear regression of $SCOR_{ara}$ against ASI for the entire time series (purple bar), the Palaeozoic (red bars) and the Triassic-Pleistocene (green bars). The strength of the correlation between $SCOR_{ara}$ and ASI changed at around the Carboniferous–Permian boundary and at the Permian–Triassic boundary, whereas no distinct point of change was found in the Mesozoic–Cenozoic time series. **b**, Linear models of SCOR ara against ASI in windows of increasing length for the Palaeozoic and for the Mesozoic–Cenozoic.

Expanding windows start with the first six stages and all the data are plotted at the last stage of the respective window. Black line, slope; blue area, R^2; diamonds, P values (only P values < 0.1 are shown). The boxes at the bottom of the graph indicate the gap for the first five stages (hatched pattern), and whether linear models were generated using ordinary least squares (OLS) or GLS (Methods). These results demonstrate a strong positive correlation between $SCOR_{ara}$ and ASI for the Palaeozoic time series, and a strong, although less robust, positive correlation in the early Mesozoic that weakens with the inclusion of data from the Middle Jurassic onwards. **c**, Predicting ASI from $SCOR_{ara}$ with CCM for expanding time series. All the included time series start with the first Ordovician stage and all data are plotted at the final stage of their respective window. The CCM prediction skills (solid black line) can be interpreted as the strength of dynamic influence of ASI on $SCOR_{ara}$. The dashed red line shows the 95th percentile of 500 random surrogate time series, which we take as a significance criterion. Time windows shorter than the Ordovician-Middle Triassic did not pass the CCM convergence test and were not included (Methods). The CCM skill shows a sustained drop when the Jurassic–Early Cretaceous stages are added, which implies a continuously weakening dynamic influence of ASI on $SCOR_{ara}$.

2. 海相铁氧化物揭示海水氧同位素的地质历史

翻译人：冯婉仪 fengwy@sustech.edu.cn

Galili N, Shemesh A, Yam R, et al. ***The geologic history of seawater oxygen isotopes from marine iron oxides****[J].* ***Science****, 2019, 365(6452): 469-47.*

摘要：自太古宙以来，海相沉积岩的氧同位素组成（$\delta^{18}O$）已经增长了 10 – 15 ‰。温度和流体 $\delta^{18}O$ 对岩石同位素组成的双重控制妨碍了这个趋势的解释。过去的 20 亿年间海相铁氧化物 $\delta^{18}O$ 的新记录也显示了一个类似的长期增长的趋势。铁氧化物的沉淀实验表明铁氧化物和水之间的氧同位素分馏与温度的变化关系不大，这说明随着时间的推移，海水 $\delta^{18}O$ 的增长是导致海相沉积物 $\delta^{18}O$ 长期增长的主要原因。^{18}O 的富集可能是由于陆相沉积盖层的增厚、高温洋壳蚀变与低温洋壳蚀变比例的变化，或者是这些因素与其他因素的结合导致的。

ABSTRACT: The oxygen isotope composition ($\delta^{18}O$) of marine sedimentary rocks has increased by 10 to 15 per mil since Archean time. Interpretation of this trend is hindered by the dual control of temperature and fluid $\delta^{18}O$ on the rocks' isotopic composition. A new $\delta^{18}O$ record in marine iron oxides covering the past ~ 2000 million years shows a similar secular rise. Iron oxide precipitation experiments reveal a weakly temperature-dependent iron oxide–water oxygen isotope fractionation, suggesting that increasing seawater $\delta^{18}O$ over time was the primary cause of the long-term rise in $\delta^{18}O$ values of marine precipitates. The ^{18}O enrichment may have been driven by an increase in terrestrial sediment cover, a change in the proportion of high- and low-temperature crustal alteration, or a combination of these and other factors.

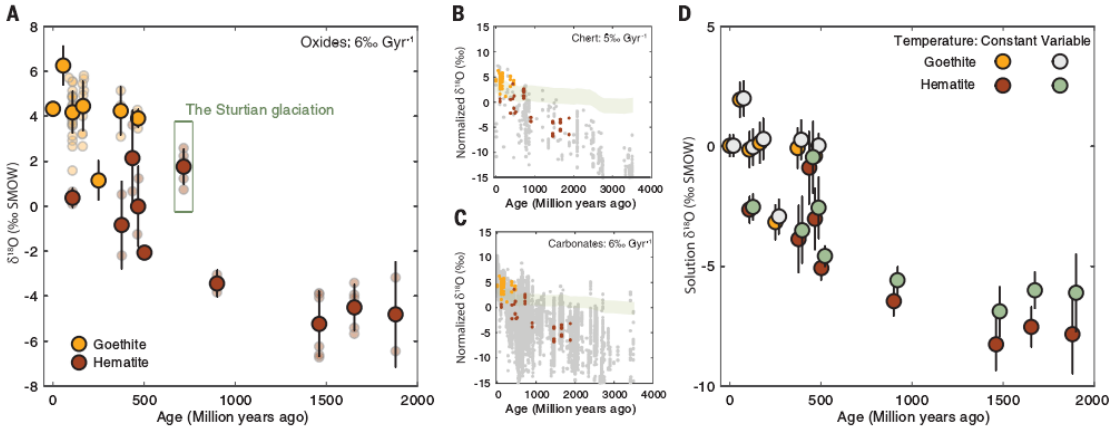

Figure 1. The new oxide $\delta^{18}O$ record. (A) Goethite (orange circles) and hematite (red circles) period average $\delta^{18}O$ values ($\pm 1\sigma$), underlain by individual measurements (small, semitransparent circles). Error bars of 0.85‰ (1σ) were assigned to data from formations where only a single sample was analyzed. (B and C) The iron oxide $\delta^{18}O$ record overlain on the (B) chert $\delta^{18}O$ record and (C) carbonate $\delta^{18}O$ record. The overlap between the iron oxide record and the chert and carbonate records serves to illustrate the similarity in slope and was achieved by subtraction of 28 and 26‰, respectively, from all the data in those records The shaded green areas in (B) and (C) represent a synthetic range of iron oxide $\delta^{18}O$ values generated from the chert and carbonate records, respectively, under the assumption of constant seawater $\delta^{18}O$ of 0‰. The slopes of linear regressions through the iron oxide, chert, and carbonate records are shown in the top-right corner of (A), (B), and (C), respectively. The chert slope was calculated using only value in the top 10th percentile, which are considered to be the best preserved. (D) The $\delta^{18}O$ of the iron oxides' parent fluids, calculated under an assumption of (i) constant temperature (15 ± 10 °C) or (ii) decreasing temperature with time [on the basis of O and Si isotopes in chert and protein reconstructions].

3. 定义大印度的边界

翻译人：刘伟 inewway@163.com

Meng J, Gilder S A, Wang C, et al. ***Defining the limits of Greater India****[J].* ***Geophysical Research Letters****, 2019, 46(8): 4182-4191.*

摘要：大印度包括印度板块的一部分，该板块俯冲到亚洲之下，形成了青藏高原。因此，确定大印度的大小是模拟印度亚洲碰撞、高原生长和新特提斯地区构造演化的一个关键约束条件。我们报告了早白垩世特提斯喜马拉雅中东部的古地磁数据，这些数据显示的古纬度与以前早白垩世的古地理重建相一致。这些数据表明，大印度从印度目前的北缘向北延伸至少 2,675±720 和 1,950±970 公里，分别为 83.6° E 和 92.4° E。通过俯冲作用消耗岩石圈面积≥ 4.7×10^6 km^2，严格限制了从冈瓦纳裂离以来印度岩石圈的最小消耗量。

ABSTRACT: Greater India comprises a part of the Indian plate that subducted under Asia to help form the Tibetan Plateau. Defining the size of the Greater India is thus a key constraint to model the India Asia collision, growth of the plateau, and the tectonic evolution of the Neo Tethyan realm. We report Early Cretaceous paleomagnetic data from the central and eastern Tethyan Himalaya that yield paleolatitudes consistent with previous Early Cretaceous paleogeographic reconstructions. These data suggest Greater India extended at least 2,675±720 and 1,950±970 km farther north from the present northern margin of India at 83.6° E and 92.4° E, respectively. An area of lithosphere 4.7×10^6 km^2 was consumed through subduction, thereby placing a strict limit on the minimum amount of Indian lithosphere consumed since the breakup of Gondwanaland.

Plain Language Summary: Greater India is part of the Indian plate, subsequently subducted under Asia, that helped create the Tibetan Plateau. The amount of Greater Indian crust therefore plays a critical role to address key problems in continental geodynamics. To what extent can continental crust be subducted? How much crust was derived from horizontal shortening of existing crust? How much of Tibet was created by subducted buoyant, continental crust? We provide paleomagnetic evidence that defines the minimum size of Greater India. Our data show that a lithospheric area of 4.7×10^6 km^2 was subducted, which supports the notion that the growth of Tibetan Plateau in the Cenozoic occurred by adding buoyant material to its base.

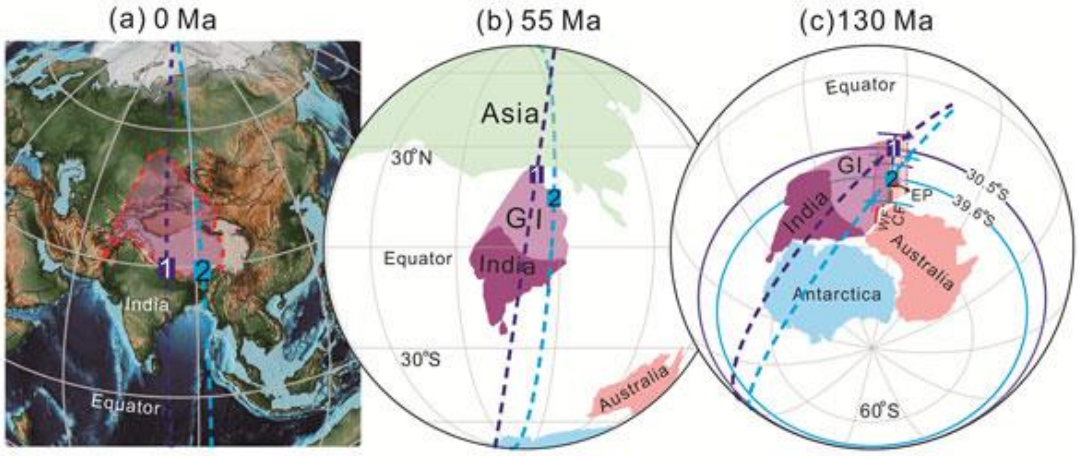

Figure 1. Paleogeographic evolution of Greater India. (a) Present day geography. Numbered squares 1 (dark blue) and 2 (light blue) correspond to the sampling locations of Zhongba and Cuona. Great circles were fit through the sampling sites along constant lines of longitude drawn in the same color. The light purple area with the red dashed line indicates the area that was occupied by Greater India, which has been subducted into the mantle, to give the reader an idea of its original extent. (b) Reconstruction at 55 Ma at the onset of the India-Asia collision when Greater India began subducting under Eurasia. (c) Reconstruction at 130 Ma showing the maximum and minimum extension of Greater India, which occurs where the great circles intersect the paleolatitudes at points 1 and 2, with uncertainties indicated by the error bars in paleolatitude and their respective crossings of the great circles. The eastern boundary of Greater India contains the Wallaby-Zenith Fracture Zone (WF), Cape Range Fracture Zone (CF), and the Exmouth Plateau (EP; Ingalls et al., 2016; Powell et al., 1988). The model assumes only N-S shortening occurred after 55 Ma. Diagrams were produced with Gplates (Boyden et al., 2011) in a paleomagnetic reference frame based on the apparent polar wander paths from Torsvik et al. (2012).

4. 西伯利亚 Viluy Traps 地区记录的泥盆纪地磁场的异常降低

翻译人：王浩森 502691781@qq.com

Hawkins L M A, Anwar T, Shcherbakova V V, et al. ***An exceptionally weak Devonian geomagnetic field recorded by the Viluy Traps, Siberia****[J].* ***Earth and Planetary Science Letters****, 2019, 506:134-145.*

摘要：探明地磁场异常行为的平均时间对于理解过去的磁层屏蔽以及推断地球深层演化至关重要。数十万至数亿年以来地磁场变化与核幔边界过程之间的联系已经提出，然而由于缺乏可靠的数据，便很难建立 267-319 百万年间的两者关系。为了提高 267-319 百万年前的记录，我们提出了多种方法从该地区的九个堤坝和熔岩流中得到古地磁记录，其结果是处于上泥盆世时期的 376.7±1.7 Ma 和 364.4±1.7 Ma 之间。这些站位中有两个站位之前已经进行了古方向的研究，其中一个得到了公认的西伯利亚 260 百万年的极点（Q 因子为 6），所有站位产生的极弱场值在 4.3-14.9 ZAm^2 之间，与中下泥盆世西伯利亚样本的其他最新结果相当吻合。QPI 标准已被用来证明这些新的古强度低值的可靠性，证实了其他西伯利亚近期研究得到的弱磁场现象，以及包含的的太阳风辐射发生率增加的时期一直延伸到上泥盆纪。除了证据泥盆纪期间出现中高反转频率以及潜在的多极分量外，这些较弱的场值还表明相对于最近的时间，穿过 CMB 的热流模式明显不同。

ABSTRACT: The detection of anomalous time averaged geomagnetic behaviour is crucial for understanding past magnetospheric shielding and inferring deep Earth evolution. Links have been suggested between geomagnetic field variation over timescales of tens to hundreds of millions of years and processes near the core–mantle boundary (CMB); however, this becomes difficult to establish prior to the Permo Carboniferous Reversed Superchron (PCRS; 267-319 Ma) due to a lack of reliable data. To improve the record prior to the PCRS, we present multi-method produced paleointensity results from nines dykes and lava flows from the Viluy Traps, Siberia, emplaced during the Upper Devonian between 376.7±1.7 Ma and 364.4±1.7 Ma. These sites have previously been published as part of two paleodirectional studies, one of which produced the accepted 360Ma pole for Siberia (Q factor 6). All of the sites produced very weak field values ranging from 4.3-14.9 ZAm^2, in close agreement with other recent results from Mid-Lower Devonian Siberian samples.

QPIcriteria have been used to illustrate the reliability of these new, low paleointensities, confirming the period of weak field suggested by other recent Siberian work, and the period of implied increased incidence of solar wind radiation, extended into the Upper Devonian. Along with evidence for moderate-high reversal frequencies and a potentially significant multipolar component during the Devonian, these weak field values also suggest a significantly different pattern of heat flow across the CMB relative to more recent times.

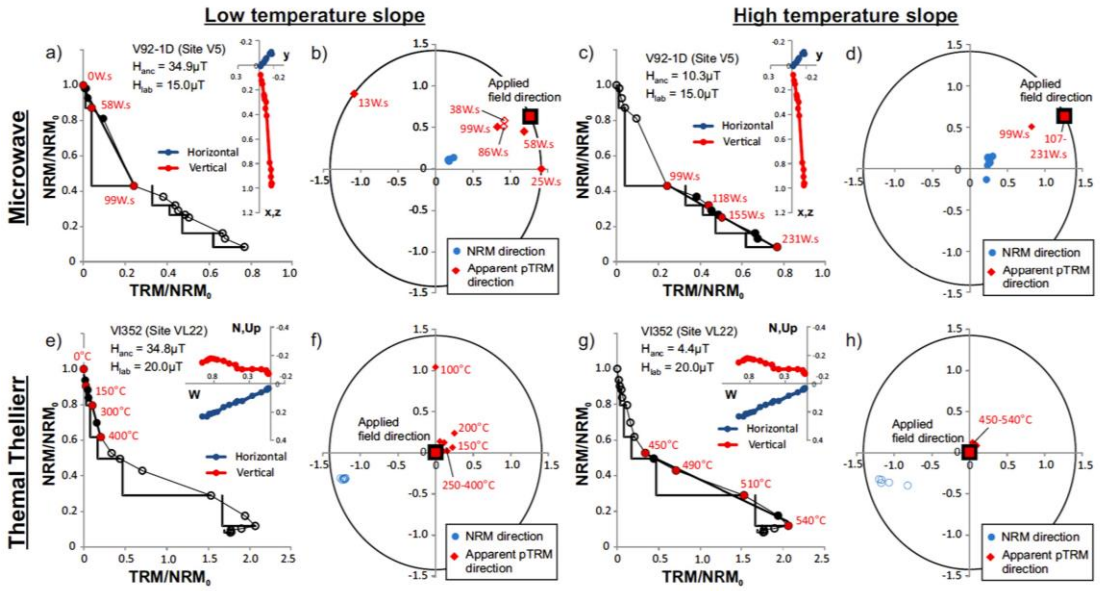

Figure 1. Examples of two-slope Arai plots, where both slopes pass selection criteria, with stereoplots showing the NRM direction of the sample and apparent pTRM directions. The samples both have Type 1 mineralogy, the only mineralogy where both slopes from the same experiment are shown to pass. The top row is a Microwave IZZI protocol example showing; a, b) the low temperature slope and c, d) high temperature slope. The bottom row is a Thermal Thellier-Coe example showing; e, f) the low temperature slope and g, h) high temperature slope. While the NRM directions do not vary significantly across the two slopes, the pTRM checks for the low temperature slope are deflected from the applied field direction; in both cases they tend toward the applied field direction with increasing power/temperature steps. The deflection of the pTRM's is not in a consistent direction, which excludes magnetic anisotropy as the cause, leaving pTRM tails as a likely explanation. For the Microwave experiment, sequential pTRM's look to differ by a high angle, sometimes >90◦, while sequential Thermal pTRM's differ by a much smaller angle. This could be due to the different protocols, with the high angle caused because of the alternating ZI and IZ steps used during the Microwave experiments. This deflection of the pTRM directions is representative of all of the low temperature pTRM behaviour observed across the different sites and magnetic mineralogy types, which is why all of the LTC's have been excluded even if they passed selection criteria.

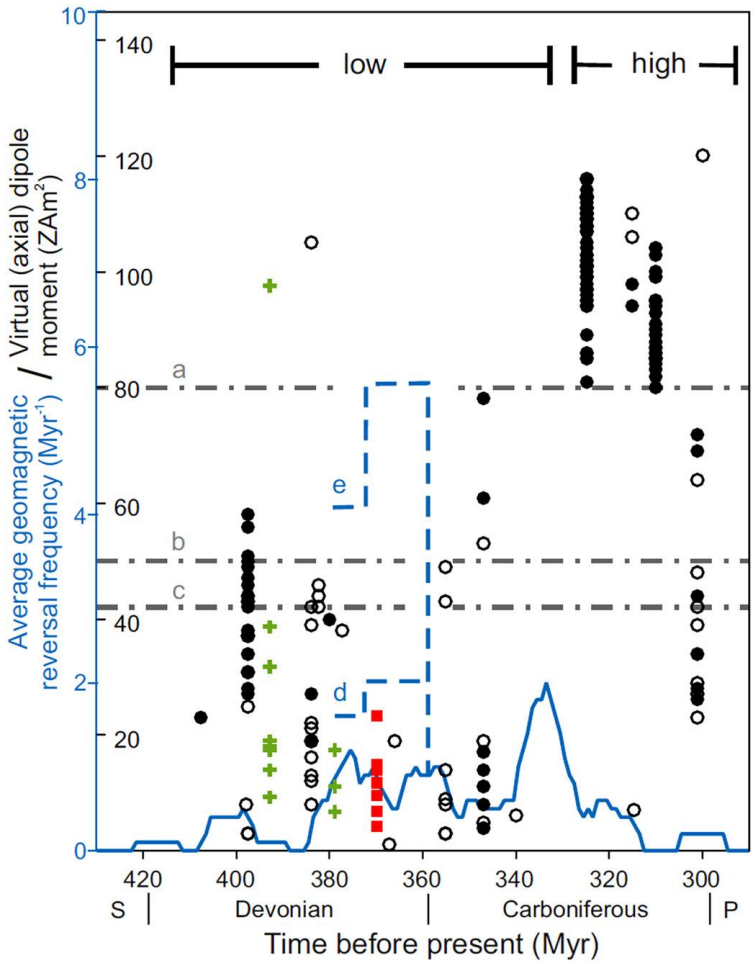

Figure 2. V(A)DM values for the Devonian–Carboniferous sites (black circles; filled have $n \geq 3$and std. dev ≤ 25%) from the PINT15 database (Biggin et al., 2009) and the World Paleointensity Database (wwwbrk.adm .yar.ru /palmag /database _e .html), with recently published data from Minusa and Kola (green crosses) and Viluy data pub-lished here (red squares). The blue line represents the average reversal frequency binned per 10 million yr (unbroken line represents the schematic Canning Basin from the GTS2016 update, which is likely to be an underestimate, and the dashed blue lines are for the d) minimum and e) maximum possible reversal frequency from Hansma et al., 2015). The dashed grey lines represent average field strength for a) the present day and the Phanerozoic average field strength from b) Biggin et al. (2015)and c) Tauxe et al.(2013).

5. 在冰期粉尘输送更多生物可利用的铁源到南大洋

翻译人：王敦繁 dunfan-w@foxmail.com

Elizabeth M. S, Gisela W, Frank L, Robert F. A, Benjamin C. B. ***Highly bioavailable dust-borne iron delivered to the Southern Ocean during glacial periods. PNAS****, 2018, 115(44):1180-1185.*

摘要：在铁含量受限的南大洋中，生物可利用的粉尘成因铁源输入的变化可通过调节浮游植物的生长和 CO_2 与有机物转化与埋藏而影响气候的变化。铁的化学形态影响其生物的可利用度，现代粉尘源中由冰川风化的的含铁矿物高度不稳定而且生物利用度较高。然而，在冰期与间冰期之间由粉尘作用输入南大洋中铁的种类是未知的；在地质时期其对生物可利用铁含量的影响也没有被量化。本文利用 x 射线吸收光谱法对冰期南大西洋和南太平洋海洋沉积物进行了研究，重建了末次冰期旋回的粉尘输入不同种类铁的形成过程，确定了冰期活动和冰期时铁的粉尘输入对生物可利用铁的影响。我们发现，作为总粉尘携带 Fe 的百分比--Fe(II)的含量在间冰期从~ 5%增加到~ 10%，而在冰期从~ 25%增加到~ 45%。不同铁的形态主要由冰川期粉尘成因的原生含铁硅酸盐矿物所决定。结果表明，冰川的物理风化作用增加了冰期到达南大洋的粉尘中生物可利用的 Fe(II)的比例，这说明冰川活动与寒冷的冰期温度之间存在正反馈关系。

ABSTRACT: Changes in bioavailable dust-borne iron (Fe) supply to the iron-limited Southern Ocean may influence climate by modulating phytoplankton growth and CO_2 fixation into organic matter that is exported to the deep ocean. The chemical form (speciation) of Fe impacts its bioavailability, and glacial weathering produces highly labile and bioavailable Fe minerals in modern dust sources. However, the speciation of dust-borne Fe reaching the iron-limited Southern Ocean on glacial-interglacial timescales is unknown, and its impact on the bioavailable iron supply over geologic time has not been quantified. Here we use X-ray absorption spectroscopy on subantarctic South Atlantic and South Pacific marine sediments to reconstruct dust-borne Fe speciation over the last glacial cycle, and determine the impact of glacial activity and glaciogenic dust sources on bioavailable Fe supply. We show that the Fe(II) content, as a percentage of total dust-borne Fe, increases from ~ 5 to 10% in interglacial periods to ~ 25 to 45% in glacial periods. Consequently, the highly bioavailable Fe(II) flux increases by a factor of ~ 15 to 20 in glacial

periods compared with the current interglacial, whereas the total Fe flux increases only by a factor of ~ 3 to 5. The change in Fe speciation is dominated by primary Fe(II) silicates characteristic of glaciogenic dust. Our results suggest that glacial physical weathering increases the proportion of highly bioavailable Fe(II) in dust that reaches the subantarctic Southern Ocean in glacial periods, which represents a positive feedback between glacial activity and cold glacial temperatures.

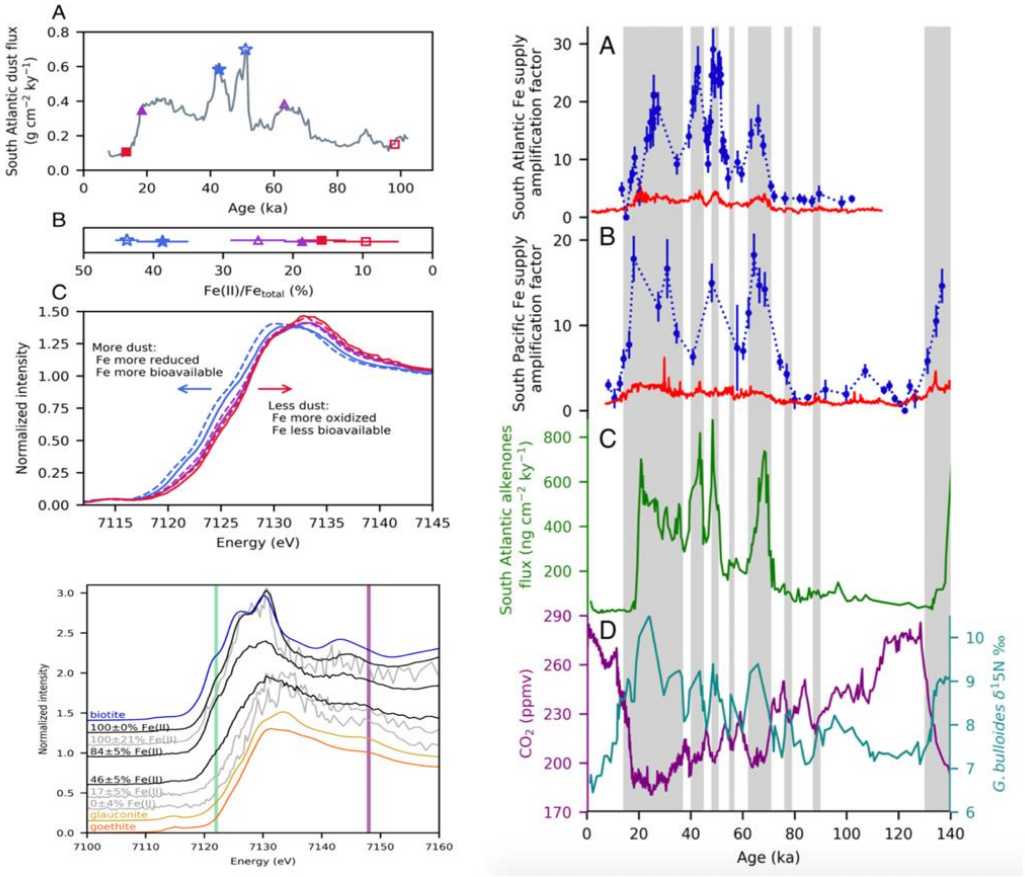

Figure 1. Right: (A) The ^{230}Th-normalized ^{232}Th-based dust flux (gray) from the South Atlantic marine sediment core (TN057-06) plotted with representative high (blue stars), medium (purple triangles), and low (red squares) dust flux samples. (B) Fe(II)/Fe total values for the representative samples calculated using LCF of the sample with mineral standards of known Fe(II) content, using the Fe K-edge k3-weighted chi function. All error bars on Fe(II)/Fe total values are based on the goodness of fit and are produced using Larch (25). The colors and open and closed symbols in A match those in B. (C) Fe K-edge XAS spectra for the representative samples. Colors in C are the same as in A and B, with dashed lines corresponding to open symbols and solid lines corresponding to filled symbols. Lower edge positions indicate Fe that is more reduced and therefore more bioavailable, and vice versa (10). Possible ice-rafted debris and other terrestrial mineral contributions to the ^{230}Th- normalized ^{232}Th dust proxy are the topic of ongoing research, especially for the high peaks in Marine Isotope Stage 3 (blue stars). And Microprobe-based XAS of individual particles in a South Atlantic core (TN057-06), at a glacial and interglacial depth. The black solid lines are μXAS of three individual particles from the glacial sediment

sample (42.7 ka), and the gray solid lines are μXAS of three individual particles from the interglacial sediment sample (92.34 ka). The spectra are labeled with their Fe(II)/Fe total concentrations. Fe(II)/Fe total was calculated using LCF of the sample with standards run contemporaneously, using the normalized intensity in the near-edge region (7,100 eV to 7,180 eV). The glacial particles were more reduced, on the whole, than the interglacial particles. A primary Fe(II) silicate standard (biotite, blue), an Fe(III) oxide/hydroxide standard (goethite, orange), and a secondary phyllosilicate standard (glauconite, goldenrod) are also plotted and labeled. The pure Fe(II) particles were > 99% biotite and hornblende [primary Fe(II) silicates]. The vertical lines guide the eye to differences in edge positions (green) and postedge features (magenta) be- tween the Fe(II) and Fe(III) rich samples. Spectra are offset for clarity(below). Left: Amplification factors for two measures of Fe supply [Fe flux in red solid lines and Fe(II) flux in blue circles connected with a dotted line] in (A) the South Atlantic (TN057-06) and (B) the South Pacific (PS75/56-1), with (C) alkenones and (D) atmospheric CO2 and foraminifera-bound δ15N records. (A and B) Amplification factors for Fe flux and Fe(II) flux show the relative in- crease from Holocene values, for each time point. Errors are propagated for Fe concentration, MAR, Fe(II)/Fe total quantification, and the Holocene Fe(II) flux estimate. Dust flux maxima corresponding to atmospheric CO_2 minima in the last glacial cycle (1) are indicated in gray shaded bars in all plots, where Fe supply and productivity is high. In C, the alkenones flux (1, 42), a productivity proxy for the subantarctic South Atlantic core TN057-06/site OPD 1090, correlates with Fe supply over the last glacial cycle. In D, the Globigerina bulloides foraminifera-bound δ15N record (1) from ODP 1090 (cyan solid line) and the atmospheric CO_2 record as recorded in Antarctic ice cores (43) (purple solid line) show the impacts of Fe fertilization over the last glacial cycle on surface nitrate utilization and climate, respectively.

6. 阿拉斯加考古炉灶的磁测：一种用来调查通往北美之路上人类存在的工具

翻译人：曹伟 11930854@mail.sustech.edu.cn

Thomas M. Urban, Jeffrey T. Rasic, Claire Alix , et al. ***Magnetic detection of archaeological hearths in Alaska: A tool for investigating the full span of human presence at the gateway to North America*** *[J].* ***Quaternary Science Reviews****, 2019, 211: 73-92.*

摘要：磁测方法在白令岛东部发现考古炉灶中显示出了巨大潜力，其应用范围包括从间歇性的露天营火到更大的热密集活动区。本文中我们将介绍该方法的概述，同时展示来自美国阿拉斯加州七个国家公园服务单位的八个支持性案例研究，涵盖了不同地理环境和历史阶段。这些案例研究共同证明了磁探测仪器在各种操作模式下寻找跨越已知人类活动范围可确定年代的考古沉积物的能力。案例范围从最简单的在“搜索模式”下使用磁强计作为单一传感器侦察，到与其他地球物理方法（如探地雷达）共同形成梯度组合，以及精确的测量结果和细致的解释。文中所举的例子从更新世开始，跨越了东白令海峡 12000 年以来的人类活动，包括新世界多个人类群体的到来、出现和扩张。

ABSTRACT: Magnetic survey methods have recently shown tremendous potential for the detection of archaeological hearths in Eastern Beringia, ranging from intermittent open-air camp fires to larger heat intensive activity areas. Here we present an overview of the method along with eight supporting case studies from seven U.S. National Park Service units in the U.S. state of Alaska, covering diverse geographic settings and time-periods. Together, these case studies demonstrate the capabilities of magnetic detection instruments in various modes of operation for finding datable archaeological deposits that span the breadth of known human occupation of this region. The examples range from the simplest use of the magnetometer as a single sensor reconnaissance instrument in a “search mode”, to use as a gradiometer in conjunction with other geophysical methods such as ground-penetrating radar, to record precise measurements and inform nuanced interpretations. Examples presented here range from the terminal Pleistocene to historic periods, spanning 12,000 years of human activity in Eastern Beringia, and encompassing the arrival, emergence, and expansion of multiple human groups or cultural traditions in the New World.

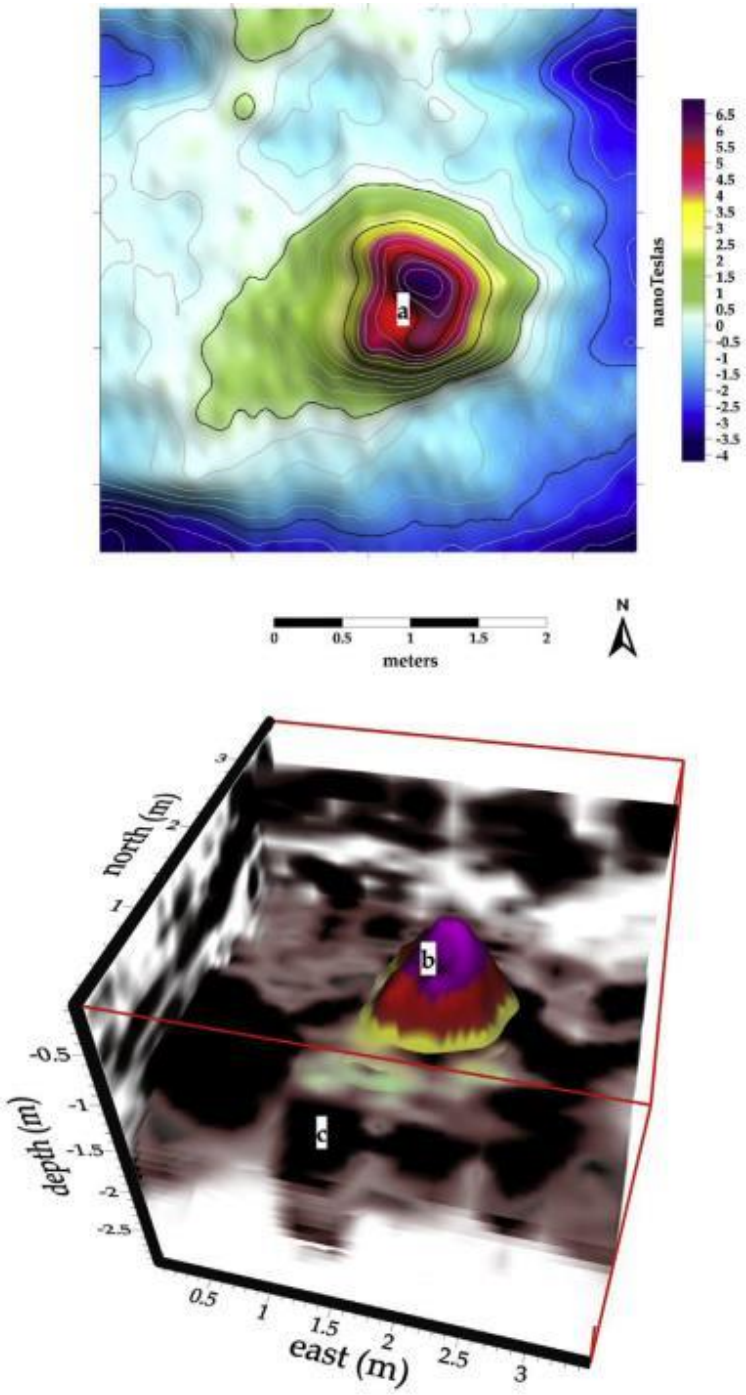

Figure 1. Top: Magnetic hearth anomaly (a) inside a house depression. Bottom: 3-D visualization of the house depression combining the magnetic anomaly from the top (b), with GPR data showing internal structural elements of the house (c).

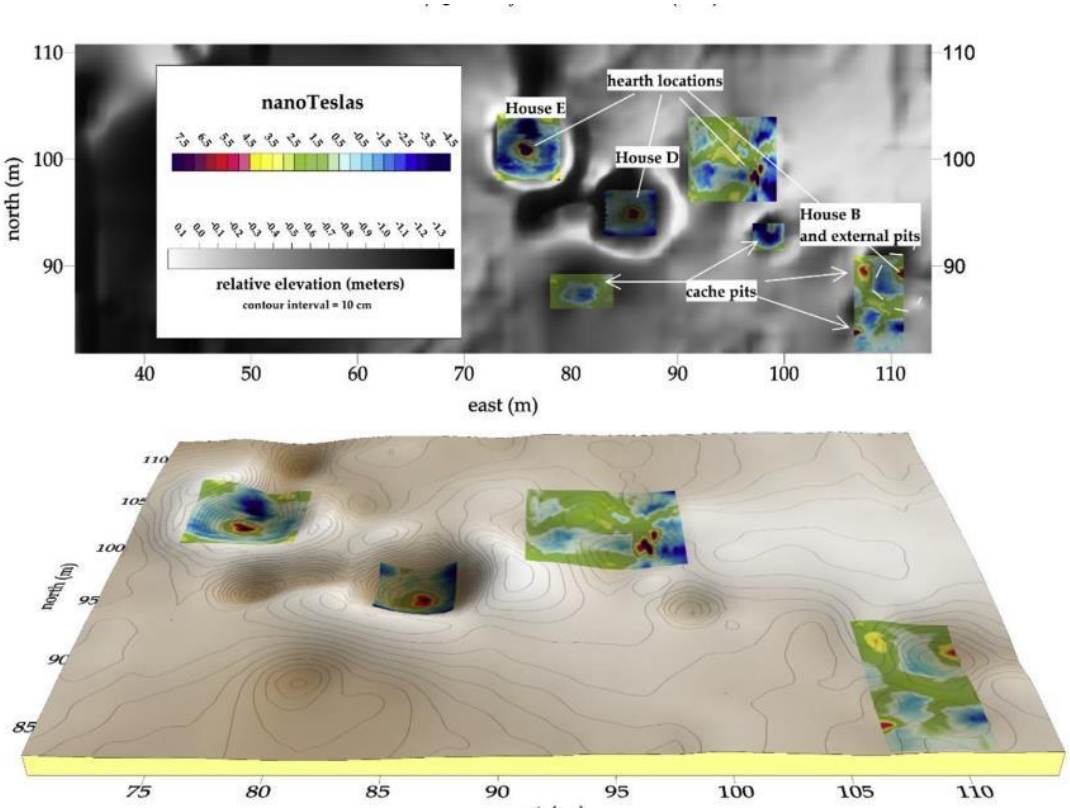

Figure 2. Hearth anomalies situated within a cluster of surface depressions. The hearth shown in Fig. 9 is indicated above in the House D depression, among a cluster of other house depressions and smaller cache pits. Some of these smaller pits are magnetized, including two of the four external pits that surround House B. This indicates that not all of these small pits had been used for the same purpose.

7. 3200 年前地中海东岸的寒旱气候灾害的爆发

翻译人：郑威 11930589@mail.sustech.edu.cn

Kaniewski D, Marriner N, Cheddadi R, et al. ***Cold and dry outbreaks in the eastern Mediterranean 3200 years ago****[J].* ***Geology****, 2019, 47(10): 933-937.*

摘要：气候能够影响社会吗？无论过去和现在，这个问题都被3200年前影响地中海的重大社会经济危机所掩盖。在青铜时代晚期和铁器时代早期（黑暗时期），爱琴海和地中海东部的核心文明如何灭亡仍然是有争议的，因为它产生了气候变化是否对古代社会有显著性影响的问题。尽管有关这种气候变化的证据在不断出现，但近来对其变化幅度量化的尝试仍不具有说服力。在此，我们着眼于经济、政治和文化变化及其剧烈的黎凡特北部（叙利亚沿海地区）。我们对过去的气候变化进行了量化，发现与当前条件相比，年平均温度有-2.3±0.3 ℃到-4.8±0.4 ℃的异常。降雨机制在季节上有显著变化，冬季降水减少了40%。历时300年的寒旱气候始于约3200年前，同时期地中海东部地区发生了深刻的社会变革。这些“小冰期”类的条件影响了农业收成，导致了严重的粮食短缺，可能因此加剧了社会政治的紧张形势。这场危机凸显了过去和现在社会对于重大的气候变化事件的脆弱性，以及它们产生的一系列后果。

ABSTRACT: Can climate affect societies? This question, of both past and present importance, is encapsulated by the major socioeconomic crisis that affected the Mediterranean 3200 yr ago. The demise of the core civilizations of the Aegean and eastern Mediterranean during the Late Bronze Age and the early Iron Age (Dark Ages) is still controversial because it raises the question of climate-change impacts on ancient societies. Although evidence for this climate shift has gradually gained currency, recent attempts to quantify its magnitude remain equivocal. Here we focus on the northern Levant (coastal Syria) where the economic, political, and cultural changes were particularly acute. We quantify past climate changes and find that mean annual temperatures attained anomalies of -2.3±0.3 °C to -4.8±0.4 °C compared to present-day conditions. Rainfall regimes displayed an important shift in seasonality, with a 40% decrease in winter precipitation. A 300 yr period of dry and cool climate started ~ 3200 yr ago and was coeval with deep social changes in the eastern Mediterranean. These “Little Ice Age”–type conditions affected harvests, leading to severe food shortages that probably aggravated the sociopolitical tensions. This crisis highlights the

fragility of societies, both past and present, to major climate-change episodes and their broader consequences.

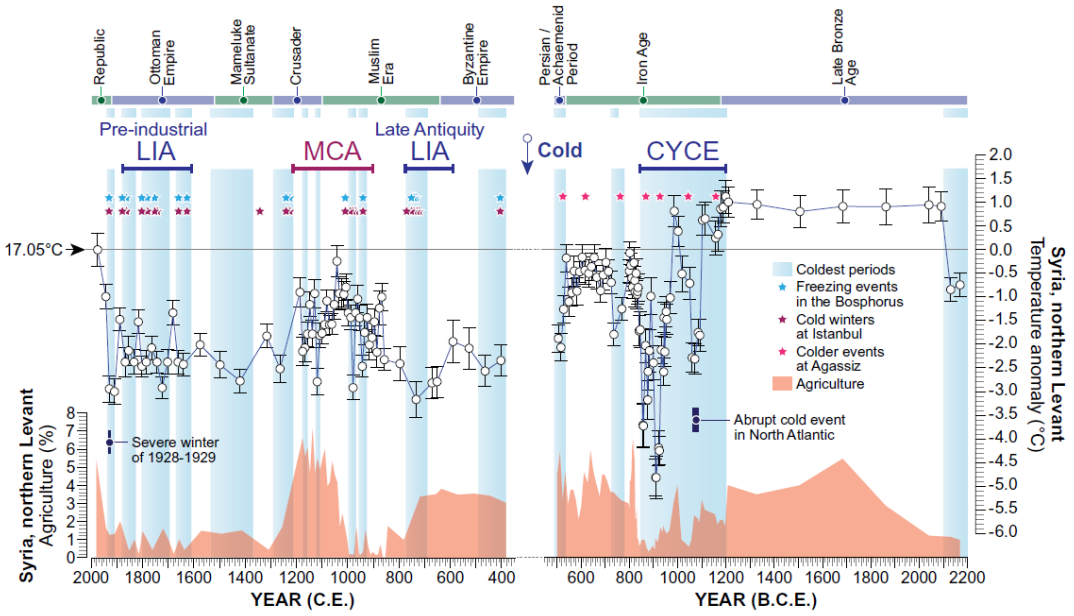

Figure 1. Reconstruction of temperature anomalies for Late Bronze Age–Persian period and Late Antiquity-20th century (with standard deviations) in Syria. Vertical blue bar highlights each cold period. Agricultural dynamics (based on cereals and viticulture) are displayed for the two periods. Percentage values are relative to the pollen sum of each sample. Blue and purple stars denote freezing events in the Bosphorus and colder winters in Istanbul (Turkey), respectively (Yavuz et al., 2007). Pink stars indicate cold events at Agassiz (Canadian High Arctic)–Greenland for the period 1200-450 BCE (Vinther et al., 2009). The abrupt cold event in the North Atlantic (event 2; Klus et al., 2018), the severe winter of 1928-1929 CE (Yavuz et al., 2007), the Late Antiquity Little Ice Age (LIA; Büntgen et al., 2016), the Medieval Climate Anomaly (MCA; Kaniewski et al., 2011a), and the pre-industrial LIA (Jones et al., 2001) are indicated. The 17.05 °C line denotes the mean annual temperature at present. Archaeological time scale has been added to the age model.

8. 末次盛冰期中国西北伊犁盆地大气风尘变化

翻译人：仲义 zhongy@sustech.edu.cn

Yue Li, Yonggui Song, Mingrui Qiang, et al. ***Atmosphere Dust Variations in the Ili Basin, Northwest China, During the last Glacial Period as Revealed by a High Mountain Loess-Paleosol Sequence [J]. Journal of Geophysical Research-Atmosphere****, 2019, 124(15), 8449-8466.*

摘要：大气风尘释放与源区气候环境密切联系。传统认为黄土沉积代表了区域性来源风尘的堆积信号，因此可以重建过去风尘-气候联系，并对于理解风尘运移、搬运和堆积的过程有很好的指示意义，然而关于中亚地区风尘释放的研究相对缺失。通过末次冰期以来中国西北部伊犁盆地的黄土剖面沉积学记录显示，砂质组分变化与沙尘暴频率较为一致，说明在 MIS2 和 MIS4 时期受到欧亚冰盖的控制，而 MIS3 时期受到夏季日照的影响。堆积速率反映了源区沉积物可利用性和沉积区植被覆盖量以及大气环流模式的综合信息。粒度和堆积速率的不一致反映出不同控制因素发生作用。对比格陵兰冰心记录和北太平洋沉积记录和中亚堆积速率显示，亚洲粉尘向下游的远距离输出通量与西伯利亚高压、大气环流的搬运效率密切相关。

ABSTRACT: Atmosphere dust emission is closely related to conditions in the source area. Typically, loess deposits represent the accumulation of locally derived dust, providing the opportunity to reconstruct past variations in dust emission and hence insights into dust-climate linkages and the underlying mechanisms of dust mobilization, transport and deposition. As yet, however, information on patterns of dust emission in Central Asia is sparse. Here we present the last glacial sedimentological data of a loess section from the frequencies of occurring strong winds, which was likely driven by Eurasian ice sheets during Marine Isotope Stage 2 (MIS2) and MIS4 and by the boreal summer insolation during MIS3. The mass accumulation rate (MAR) reflects an integration of sediment availability in the provenance, vegetation cover in the deposition area, and wind regime. The differences of driving factors potentially explain the observed mismatches between variations in grain size and MAR. Comparison of dust fluxes observed in Greenland ice core and the North Pacific deep-sea sediment with the Central/East Asian MAR records supports the idea that the high flux of long-distance export of Asian dust is closely associated with the Siberian High and also influenced by changes in the atmospheric transport efficiency and likely by

the source strength.

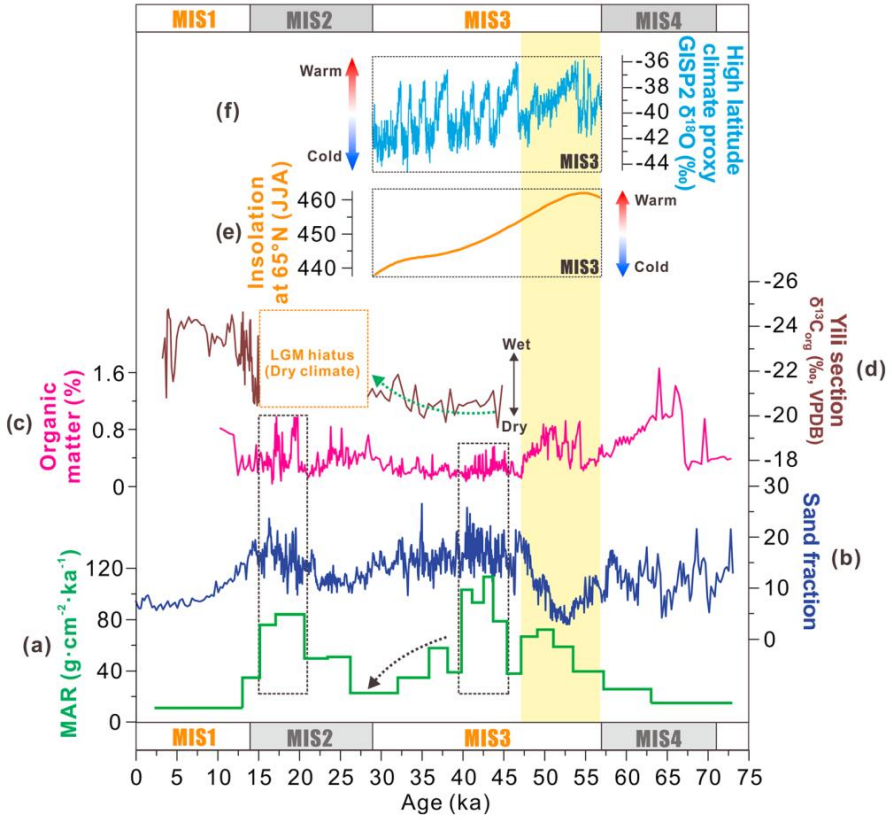

Figure 1. Comparison of variations in the mass accumulation rate (MAR; a), sand fraction (b), and organic matter content (c; supporting information) of the NLK section with $\delta^{13}C_{org}$ variations in the Yili section (Zhao et al., 2019; d), summer (June, July, and August [JJA]) insolation at 65°N (Laskar et al., 2004; e), and $\delta^{18}O$ variations from the Greenland ice cores (Rasmussen et al., 2014; f). The two black dotted boxes mark intervals in which the higher MARs correspond to the stronger winds and relatively high organic matter contents. The orange dotted box indicates the hiatus in the Yili section (Zhao et al., 2019), which suggests a dry climate prevailed in the Yili Valley during the Last Glacial Maximum (LGM; Zhao et al., 2013). The yellow dash area marks the early MIS3 in this study.

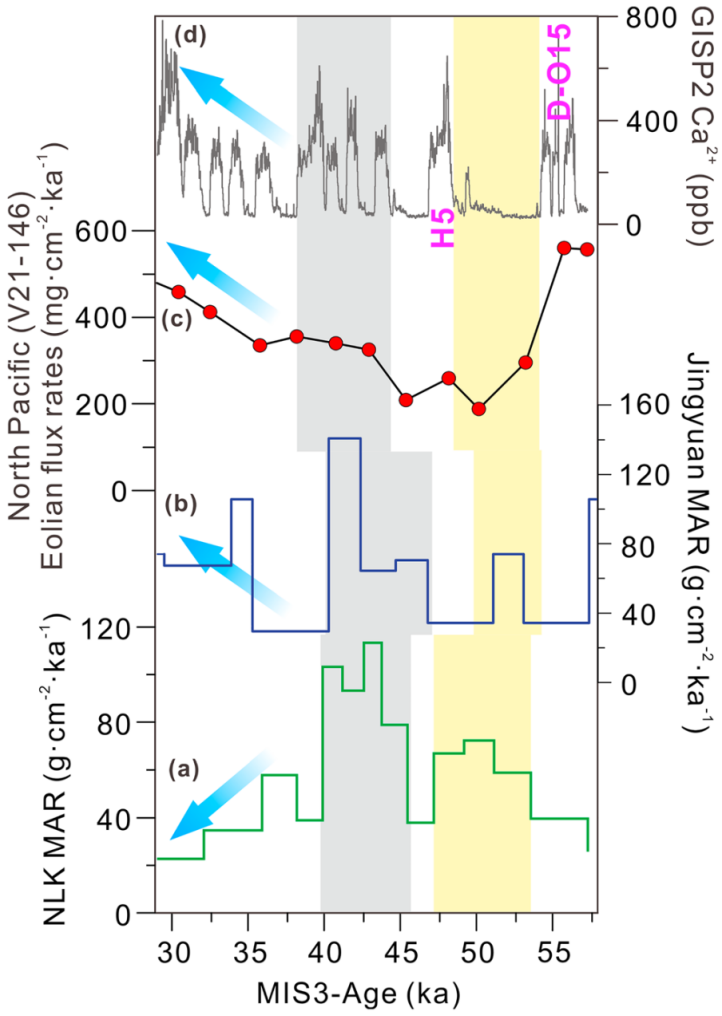

Figure 2. Comparison of eolian dust fluxes of the Nilka (NLK) section (a) with mass accumulation rates (MARs) of Jingyuan loess section, northwestern Chinese Loess Plateau (Sun, Wang, et al., 2010; b), the midlatitude North Pacific Ocean (Hovan et al., 1991; c), and dust concentrations of Greenland Ice Sheet Project 2 (GISP 2) ice core (Mayewski et al., 1997; d). We used a mean bulk density value of 1.48 g/cm3 for calculating the MARs of Jingyuan section, as Kang et al. (2015).

9. 转换边缘高原

翻译人：李园洁 liyj3@sustech.edu.cn

Loncke L, Roest W R, Klingelhoefer F, et al. ***Transform marsginal plateaus****[J].* ***Earth-Science Reviews****, 2019: 102940.*

摘要：多数海底高原在大陆到大洋过渡带表现为显著高地形。由于它们靠近大陆，通常被称为“边缘高原”，尽管这个术语定义不清楚，也没有和特殊地质或地球动力过程关联。直到现在，这种高地形被解释为从大陆分离的水下减薄大陆碎片，热点形成的玄武岩堆，火山边缘或大洋高原。很多高原形成于与不同年龄大洋盆地的转换边缘。我们第一次定义并综述与地质构造有关的一类边缘高原：“转换边缘高原”（TMPs）基于汇编的全球 20 个 TMPs，我们发现大多数转换边缘高原具有多期历史并经受过至少一次大的火山期。我们认为到目前为止热点，火山活动和转换边缘之间存在着未被发现的密切关系。由于转换边缘高原的多期历史，可能存在连续盆地和遗漏的长期存在的沉积物遗迹。这些 TMPs 在转换板块边缘垂直或斜交于周围的裂谷，很多 TWPs 在大陆裂解最后时期的最终连接点附近，可能在大陆之间形成路桥或高地形。因此，我们讨论了更广泛的科学问题，比如 TMPs 在记录和研究洋流的启动和变化或过去生物多样性的发展，生物联系和宗系进化。

ABSTRACT：Numerous submarine plateaus form highstanding bathymetric highs at continent to ocean transitions. Due to their proximity to continents, they have been frequently labelled “marginal plateaus”, although this term has not been clearly defined or associated with a specific geology or geodynamic process. Until now, these elevations have been interpreted as submerged thinned continental fragments detached from continents, basaltic buildups formed by hotspots, volcanic margins or oceanic plateaus. Many of these plateaus formed at transform margins connecting oceanic basins of contrasted ages. We propose for the first time to define and review a class of marginal plateaus related to a specific tectonic setting: “Transform Marginal Plateaus” (TMPs). Based on a compilation of 20 TMPs around the world, we show that most of them have a polyphased history and have undergone at least one major volcanic phase. Our review highlights in particular a hitherto unrecognized close link between hotspots, volcanic activity and transform margins. We also propose that, due to their polyphased history, TMPs may contain several successive basins and

overlooked long-lived sedimentary archives. We finally highlight that, because these TMPs were transform plate boundaries perpendicular or oblique to surrounding rifts, many of them were close to last-contact points during final continental breakup and may have formed land bridges or bathymetric highs between continents. Therefore, we discuss broader scientific issues, such as the interest of TMPs in recording and studying the onset and variations of oceanic currents or past biodiversity growth, bio-connectivity and lineage evolution.

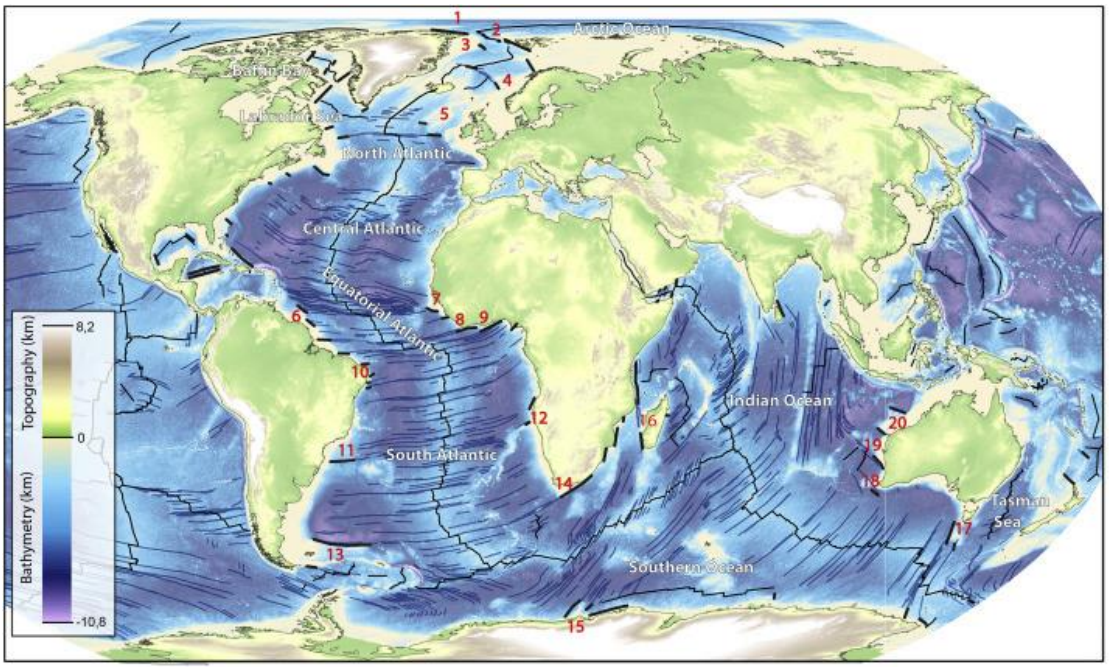

Figure 1. Location of Transform Marginal Plateaus (TMPs) on a world bathymetric and topographic map (ETOPO-1 model, Amante and Eakins 2009). Transform margins are underlined by a black thick line (from Mercier et al. 2016) (see also the TMP KML file in supplementary data). In blue, oceanic fracture zones from Matthews et al., 2011. 1. Morris Jesup Rise; 2: Yermarck; 3: NE Greenland; 4: Vøring Plateau; 5: FaroeRockall; 6: Demerara; 7: Guinea; 8: Liberia; 9: Côte d'Ivoire-Ghana; 10: Potiguar; 11: Sao Paulo; 12: Walvis; 13: Falklands-Malvinas; 14: Agulhas; 15: Gunnerus Ridge; 16: Morondava, 17: Tasman; 18: Naturaliste; 19: Wallaby-Cuvier; 20: Exmouth

10. 有机碳流控制海洋沉积物中磁小体化石的形貌

翻译人：芦阳 luyang_sz@foxmail.com

Yamazaki T, Kawahata H. ***Organic carbon flux controls the morphology of magnetofossils in marine sediments****[J].* ***Geology****, 1998, 26(12): 1064-1066.*

摘要： 趋磁菌在体内产生磁铁矿链，生物磁铁矿有特征的形貌和尺寸，受到严格的生物控制。作者检测了太平洋深海沉积物中的细菌磁铁矿化石（磁小体化石）的形貌和它们与有机碳流的关系。在相对氧化的条件中，沉积物中的磁小体化石主要为各向同性的晶体，而在更还原的条件中是各向异性的晶体为主。本文的发现对生物矿化过程有重要意义，验证了磁小体化石形貌作为古环境指标的潜力。

ABSTRACT: Magnetotactic bacteria produce chains of magnetite crystals within a cell. Bacterial magnetites have characteristic morphologies and sizes that are strictly biologically controlled. We examined morphologies of fossil bacterial magnetites (magnetofossils) preserved in Pacific deep-sea sediments and their relations to organic carbon fluxes. Isotropic crystals dominate magnetofossils in sediments in relatively oxidized conditions, and anisotropic crystals predominate in more reduced conditions. Our finding has important implications for biomineralization processes and demonstrates the potential of magnetofossil morphology as a paleoenvironmental indicator.

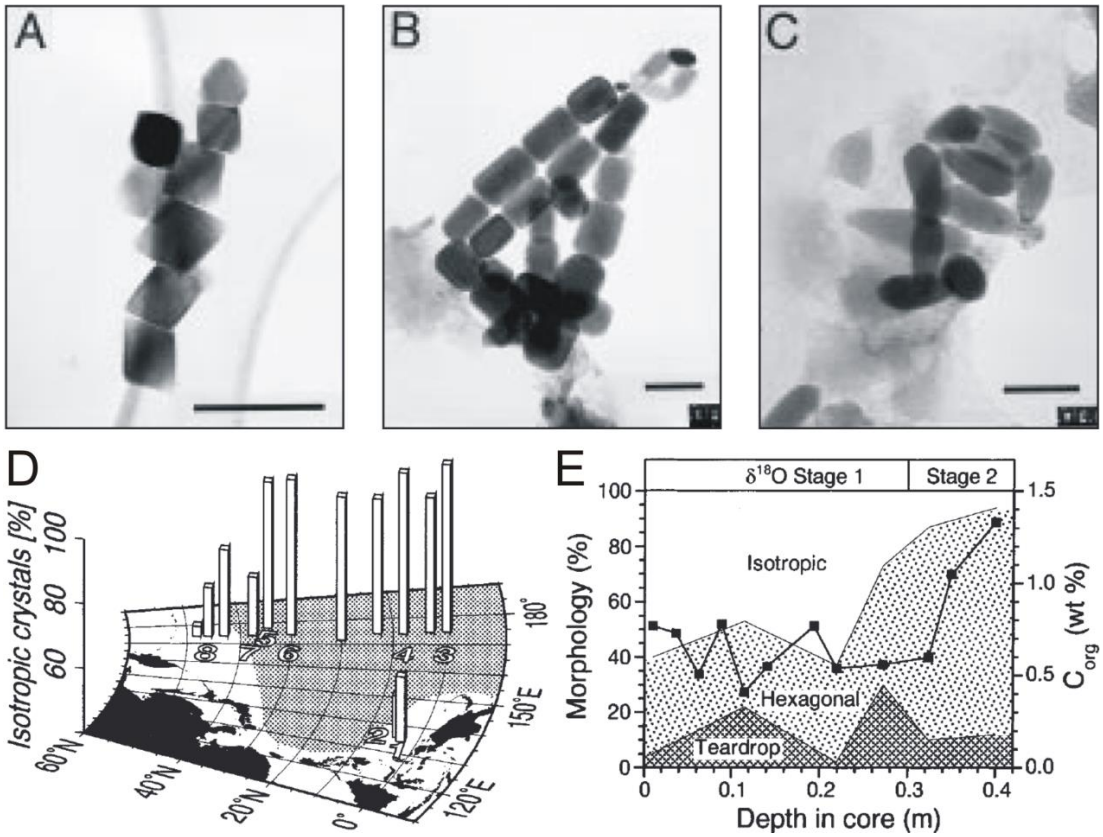

Figure 1. A-C, Typical morphologies of magnetofossils in Pacific deep-sea sediments under transmission electron microscope images. A: Isotropic, octahedron. B: Anisotropic, hexagonal prisms. C: Teardrops. Scale bars = 100 nm. D, Geographical variations of ratio of isotropic magnetofossils in surface sediments. Region dominated by isotropic crystals generally coincides with low primary productivity provinces; area having productivity of C lower than 60 g/m_2/yr is shaded (Berger and Herguera, 1992). E, Downcore variations of magnetofossil morphology within box core of hemipelagic terrigenous mud (site 1 in Figs. 2 and 3) in West Caroline basin. Glacialinterglacial transition (the oxygen isotope stage 1-2 boundary) occurs at about 0.3 m (Kawahata and Suzuki, 1994). Content of C_{org} (squares) is higher below boundary (Kawahata and Suzuki, 1994), where anisotropic, hexagonal prisms dominate magnetofossils.